On Determining the Onset and Strength of Breaking for Deep Water Waves. Part II: Influence of Wind Forcing and Surface Shear

MICHAEL L. BANNER AND JIN-BAO SONG

School of Mathematics, The University of New South Wales, Sydney, New South Wales, Australia

(Manuscript received 26 June 2001, in final form 14 January 2002)

ABSTRACT

Part I of this study describes the authors' findings on a robust threshold variable that determines the onset of breaking for unforced, irrotational deep water waves and proposes a means of predicting the strength of breaking if the breaking threshold is exceeded. Those results were based on a numerical study of the unforced evolution of fully nonlinear, two-dimensional inviscid wave trains and highlight the fundamental role played by the nonlinear wave group dynamics. In Part II the scope of these calculations is extended to investigate the additional influence of wind forcing and background shear on the evolution to breaking.

Using the methodology described in Part I, the present study focuses on the influence of wind forcing and vertical shear on long-term evolution toward breaking or recurrence of the maximum of the local energy density within a wave group. It investigates the behavior of a dimensionless local growth rate parameter that reflects the mean energy flux to the energy maximum in the wave group and provides a clearer physical interpretation of the evolution toward recurrence or breaking. Typically, the addition of the wind forcing and surface layer shear results in only small departures from the irrotational, unforced cases reported in Part I. This indicates that nonlinear hydrodynamic energy fluxes within wave groups still dominate the evolution to recurrence or breaking even in the presence of these other mechanisms. Further, the calculations confirm that the breaking threshold for this growth rate found for unforced irrotational wave groups in Part I is also applicable for cases with wind forcing and shear typical of open ocean conditions. Overall, this approach provides an earlier and more decisive indicator for the onset of breaking than previously proposed breaking thresholds and suggests a foundation for predicting the strength of breaking events.

1. Introduction

It is well known that wind-driven ocean waves have a strong group structure. This is evident in wave height records and even to the casual observer. An important feature of these evolving wave groups is the intermittent occurrence of very steep individual waves that can present hazardous conditions for shipping and offshore structures, especially if these waves break. Donelan et al. (1972) and Holthuijsen and Herbers (1986) provide compelling observational accounts that link wave breaking and the group structure of wind waves. Among the many fundamental scientific issues that arise in this context are the relative importance of wind forcing of the waves and also the influence of the concomitant vertical shear in the surface layer region through which the waves propagate.

Part I of this study (Song and Banner 2002) addresses the issue of wave breaking onset in nonlinear wave groups in the absence of wind forcing and background shear. It focuses on identifying and quantifying the role of the nonlinear hydrodynamics in the idealized case of two-dimensional irrotational wave group evolution. It provides an extensive literature review of the topic and proposes new methodologies for quantifying the complex nonlinear behavior of three classes of initial wave group structures. Of particular relevance to the discussion of wind-forced waves and the statistics and structure of extreme waves in such wave groups are the papers of Longuet-Higgins (1984), Boccotti et al. (1993), and Phillips et al. (1993). These papers, however, do not address the underlying issue of determining the onset of wave breaking. The main body of published work on wave breaking onset has been concerned with hydrodynamical aspects and this aspect is addressed in Part I.

Historically, there have been relatively few papers that have focused on wind influence on wave breaking. One notable example was the model of Banner and Phillips (1974), who proposed that the wind drift current at the air–water interface could destabilize water waves by accelerating the onset of the kinematic condition where the horizontal water particle velocity at the wave crest attained the phase speed of the wave form. In that model, we note that the wind is regarded as only generating the wind drift current. This hydrodynamic source is then

Corresponding author address: Dr. Michael L. Banner, School of Mathematics, The University of New South Wales, Sydney 2052, New South Wales, Australia.
E-mail: m.banner@unsw.edu.au

responsible for the onset of breaking, with the direct aerodynamic forcing regarded as of secondary importance. The motivation for this model had its origin in seeking to explain the remarkably strong attenuation of small-scale wind waves by longer waves in laboratory wind wave tanks, as investigated by Phillips and Banner (1974). A number of authors, notably Wright (1976), Donelan (1987), and Chen and Belcher (2000) have subsequently questioned the primary role of the wind drift current in this process and have proposed alternative mechanisms. Observations of the influence on short waves due to the transient passage of long waves (e.g., Chu et al. 1992) reveal a very fast interaction time with strong breaking of the short waves, indicating a hydrodynamic rather than aerodynamic origin for the short wave attenuation. As this aspect remains to be fully understood, this important phenomenon cannot yet be regarded as fully resolved.

Such studies have focused on elucidating specific mechanisms in established wind wave fields. A different approach addressing the initial spectral development of sideband instabilities was investigated in two recent observational papers that contribute authoritative theoretical and observational insight into the unforced and wind-forced evolution of nonlinear deep water wave trains, focusing particularly on the initial growth rates of sideband instabilities. In their first paper, Tulin and Waseda (1999) investigate the initial evolution and related aspects of the initial instability of deep water wave trains in the absence of wind forcing, while their companion paper, Waseda and Tulin (1999) examines the additional influence of wind forcing. Contrary to earlier results reported by Bliven et al. (1986) and Li et al. (1987), their results for wind forcing showed that wind did not inhibit the growth of sidebands in the case of either two-dimensional or three-dimensional instabilities. Overall, Waseda and Tulin (1999) reported two independent effects of the wind:

1) a modification of the inviscid growth rates for a given modulational frequency, as shown by comparison with ''seeded'' experiments where initial disturbances are introduced by a prescribed wave paddle motion in the absence of wind;
2) a change in the natural modulational frequency appearing in the presence of wind that is a function of the wave age, as observed in ''unseeded'' experiments where only wind-generated waves were involved.

Waseda and Tulin conclude that it is the combination of both effects that determines whether the modulational instability is enhanced or suppressed and that, for moderate to old windsea waves, the net effect of wind on the modulational instability is small.

Our present investigation is concerned with the long-term evolution to recurrence or breaking onset and is therefore complementary to the earlier studies (e.g., Tulin and Waseda 1999; Waseda and Tulin 1999) that were concerned primarily with initial instabilities. In Part I of our investigation, we report the results of our numerical investigation of *unforced* long-term evolution of nonlinear deep water wave groups, with a major focus on (i) determinants of breaking event onset, (ii) how far in advance can wave breaking events be predicted, and (iii) what controls their strength. Part I also contains a detailed presentation of our computational approach and the reader is referred to that paper for full details of the methodology used.

Before addressing the issue of wind forcing, we recall that the complementary issue of surface layer shear is another potentially important background process that has been associated with the destabilization of wave trains. The results of Teles da Silva and Peregrine (1988) and Millinazzo and Saffman (1990), among others, suggest that the presence of linear background vertical shear has a potentially strong influence on the structure of a wave train. This was confirmed in Banner and Tian (1998, henceforth BT), for the unforced case, where the wave steepness at breaking was reduced by up to $O(20\%)$ in the presence of a strong linear vertical shear current. Our improved computational methodology and revised interpretation of the underlying energetics associated with breaking onset motivated an extension of our investigation to include an assessment of the influence of a linear surface layer shear more typical of well-developed open ocean wave conditions.

In Part II, therefore, we investigate how wind forcing and surface layer shear modify the unforced results reported in Part I, both as separate influences and when both operate concurrently. This allows an assessment of the relative importance of wind forcing and surface layer shear in relation to the fundamental nonlinear fluxes operative in the absence of wind forcing and vorticity.

2. Methodology

To avoid unnecessary duplication, the reader is referred to Part I for a detailed description of our approach and methodology, including the definitions of diagnostic variables, computational techniques, and accuracy. The additional details describing the modeling of wind forcing and surface layer shear in the calculations are given in the appropriate sections below.

3. Influence of wind forcing

To simulate the influence of wind forcing, we introduced into the free surface dynamic boundary condition in the Dold and Peregrine (1986, henceforth DP) model a surface pressure distribution persistent in phase with the wave slope, thereby ensuring positive momentum and energy fluxes to the wave field. There are various possible formulations for an imposed surface distribution in phase with the wave slope, which is necessary for sustained wind input to the wave field (e.g., Phillips

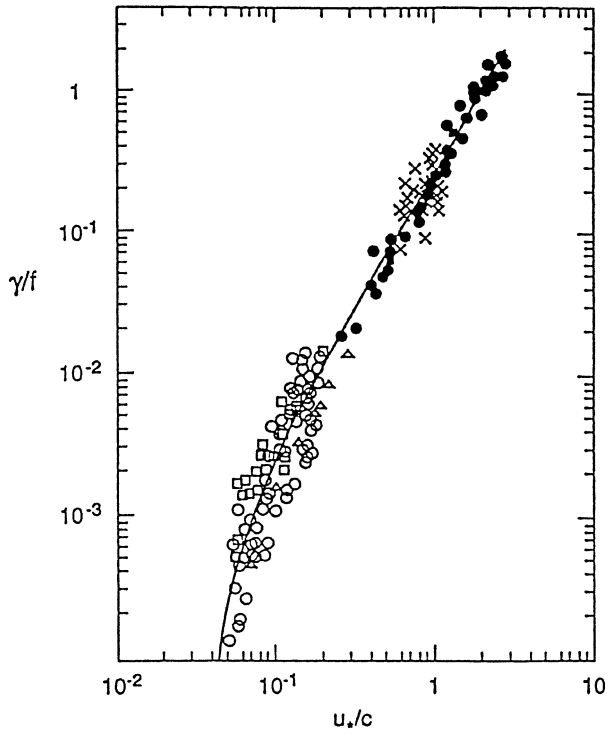

FIG. 1. Observed nondimensional wind wave growth rates against the inverse wave age. Open circles and squares are field data; other symbols represent laboratory data. Cited from Komen et al. (1994).

1977, p. 49; Donelan 1999, sec. 2). In the present study, we assumed a surface pressure distribution of the form

$$p_s(x, t) = \alpha\rho_a u_*^2 \eta_x(x, t)$$

where η specifies the free surface, α is a empirical constant (to be specified), ρ_a is the air density, and u_* is the wind friction velocity. The total energy and momentum fluxes input from the wind are respectively $\langle p_s \partial\eta/\partial t\rangle$ and $\langle p_s \partial\eta/\partial x\rangle$, where angle brackets represent an appropriate spatial, temporal, or ensemble average. In our model calculations, the magnitude of the pressure was chosen by relating the expression for the effective wind input growth rate to growth rates observed for ocean and laboratory wind waves. Figure 1 shows a compilation of these observational results in nondimensional form and the interested reader is referred to the discussion in Plant (1982) and Komen et al. (1994, sec. II. 2.3). The observed spectral wind input growth rate at frequency ω is commonly specified in the context of a Fourier decomposition of the wave surface and surface pressure fields, as discussed in detail by Donelan (1999, §2). The spectral growth rate γ is usually normalized by the wave frequency ω or f $(=\omega/2\pi)$ and expressed as a function of the inverse wave age u_*/c, where c is the corresponding wave phase speed. With reference to Fig. 1, the inverse wave age range $u_*/c < 0.2$ embraces most reported wind sea situations, from very old to extremely young, while the range $u_*/c > 0.2$ is more relevant to short fetch wave tank conditions. In the present narrow bandwidth application, c is taken as the linear phase speed of the carrier wave, assumed constant. Finally, we note that, since there is no dissipation in the DP code, there will be a continuous accumulation of energy supplied from the wind so that exact recurrence is not possible and recurrence in this context refers implicitly to a near recurrence to the initial wave group structure.

The relationship between the unknown coefficient α and the nondimensional spectral wind wave growth rate γ/f is readily established. For the surface pressure distribution proposed above, decomposing η as the linear superposition of sinusoidal traveling surface gravity wave modes and taking $\eta_t = c\eta_x$ and following Donelan (1999, §2), it is easily shown that the nondimensional spectral wind input growth rate γ, normalized by the wave frequency f, is related to α and the inverse wave age u_*/c by

$$\gamma/f = 2\pi\alpha(\rho_a/\rho_w)(u_*/c)^2.$$

From Fig. 1, with $\rho_a/\rho_w = 0.001225$, we have $\alpha \sim 32.5$ for $u_*/c \sim 0.2$. The scalings for g, ρ_w, k, and c specified above for the DP code provided scaled values of the surface pressure forcing level $\alpha_* = \alpha\rho_a u_*^2$ corresponding to different wave age conditions. Also, following Part I, the reference period T of the carrier waves is taken as 2π. In our computations, we examined the influence of α_* over the range (0.0001, 0.0016), which corresponds to u_*/c in the range (0.05, 0.2). This range of inverse wave ages spans the ocean wind wave regime from very young to very old windseas. Figure 2 illustrates the influence of the magnitude α_* of the surface pressure in modifying the surface shape and enhancing the onset of wave breaking. This example is for the unforced marginal recurrence case I group structure with $N = 5$ and $s_0 = a_0k_0 = 0.111$, for which the surface profiles at various times were shown previously in Fig. 1 of Part I. The evolution under moderate surface pressure forcing ($\alpha_* = 0.0002$) that preserves the recurrence is shown in the left-hand panels of Fig. 2. The initial profile (Fig. 2a) evolves to the peak of the recurrence cycle at $t/T = 82.9$, with the end of the recurrence cycle at $t/T = 125.7$. When the surface forcing level was increased to $\alpha_* = 0.0003$, breaking now occurs at $t/T = 82.9$ and the corresponding evolution of the surface profile is shown in the right-hand panel figures of Fig. 2. Thus for this initial wave group geometry, it is seen that increasing the applied pressure accelerates the onset of breaking. The case of an even stronger level of surface forcing, $\alpha_* = 0.0016$, resulted in accelerated wave breaking onset at $t/T = 74.6$. Following BT, the wave steepness at breaking, $(ak)_{\text{br}}$, is taken as the product of the local wavenumber and one-half of the elevation of the crest above the mean trough level and was found to increase marginally from $(ak)_{\text{br}} = 0.3328$ for $\alpha_* = 0.0003$ to $(ak)_{\text{br}} = 0.3484$ for $\alpha_* = 0.0016$. From results such as those shown in Fig. 2, we concluded that wind

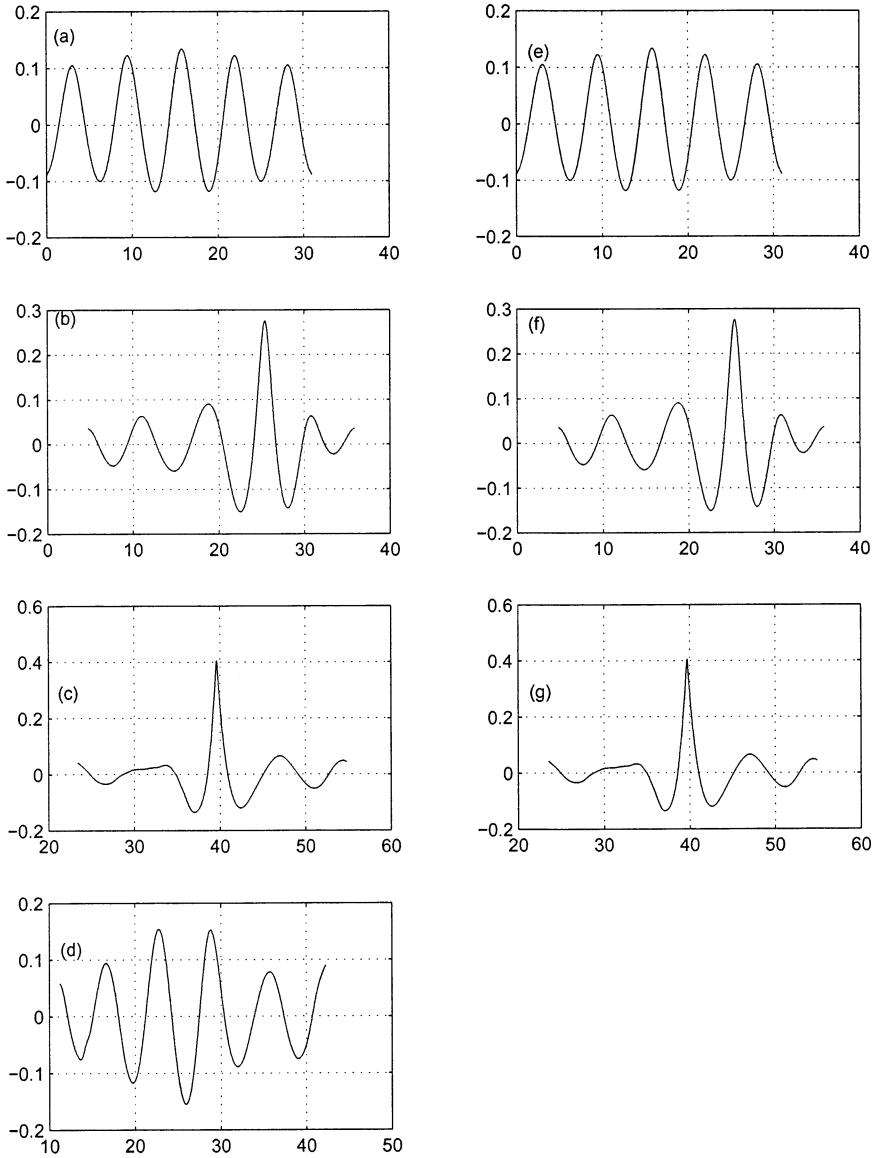

FIG. 2. Surface profiles showing the influence of the surface pressure ($p_s = \alpha_* \eta_x$) in enhancing the onset of wave breaking for case I with $N = 5$ and $s_0 = 0.111$. The reference period T of the carrier waves is 2π. (a)–(d) The evolution for pressure forcing with $\alpha_* = 0.0002$: (a) $t/T = 0$, (b) $t/T = 60$, (c) $t/T = 82.9$, (d) $t/T = 125.7$. (e)–(g) The evolution for pressure forcing with $\alpha_* = 0.0003$: (e) $t/T = 0$, (f) $t/T = 60$, (g) $t/T = 82.9$. The axes show lengths in meters.

forcing only marginally modified the geometry of the wavy surface for surface forcing levels consistent with very young to very old windseas.

Of greater significance and interest is the evolution of the diagnostic energy-related nondimensional parameters $\mu(t)$, its local average $\langle \mu(t) \rangle$ and the corresponding growth rate $\delta(t)$ that were defined in section 3d of Part I and subsequently investigated in detail for unforced, irrotational wave groups. Figure 3 shows the influence of surface forcing on $\langle \mu(t) \rangle$ and $\delta(t)$ for the three cases $\alpha_* = 0.0002$, 0.0003, and 0.0016. It is seen that the addition of surface forcing of strength $\alpha_* = 0.0002$ marginally increases the maximum value of $\langle \mu(t) \rangle$ at the peak of the recurrence cycle, but creates negligible change in the corresponding growth rate $\delta(t)$. Only for stronger wind forcing $\alpha_* = 0.0003$ does $\delta(t)$ exceed the breaking threshold δ_{th} in the range $(1.30–1.50) \times 10^{-3}$ proposed in Part I on the basis of our results for unforced evolution. Stronger wind forcing results in a faster evolution of $\langle \mu(t) \rangle$, earlier exceeding of the breaking threshold δ_{th} and a higher value of the growth rate $\delta^{\max}$ just prior to breaking.

We also examined an unforced case (case I, $N = 5$ and $s_0 = 0.12$) just beyond the recurrence limit so that

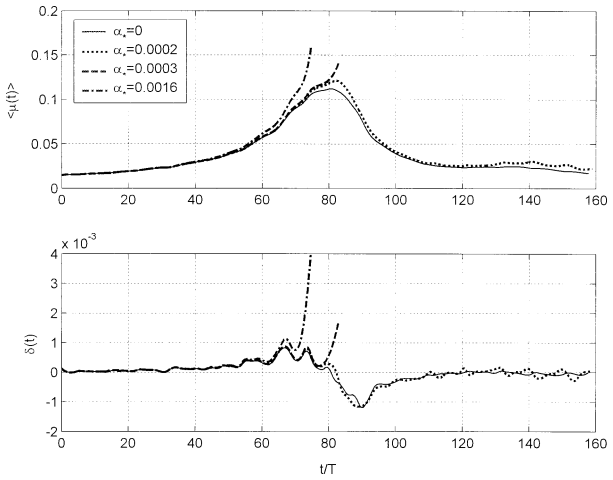

FIG. 3. The influence of wind forcing strength on the evolution of the diagnostic parameter $\langle\mu\rangle$ and its associated growth rate $\delta(t)$ for case I with $N = 5$, $s_0 = 0.111$ and several surface forcing levels $\alpha_* = 0$, 0.0002, 0.0003, and 0.0016.

breaking occurs for the unforced case. For this case, the influence of surface forcing accelerates the onset of wave breaking, with the time to breaking decreasing from $t/T = 60.5$ for $\alpha_* = 0$ to $t/T = 58.7$ and 58.4 for $\alpha_* = 0.0004$ and 0.0016, respectively. The results for $\langle\mu(t)\rangle$ and $\delta(t)$ comparing zero surface forcing ($\alpha_* = 0$) and strong surface forcing ($\alpha_* = 0.0016$) are included subsequently in Fig. 5, which also shows the comparative influence of shear. The steepness at breaking $(ak)_{\text{br}}$ increases from 0.3437 for $\alpha_* = 0$ to 0.3583 for $\alpha_* = 0.0016$. Table 1 contains a summary of the salient results.

While the intuitive expectation is that surface forcing destabilizes the motion of the wave group and accelerates the onset of breaking, we found cases where the opposite can occur. In some cases, an unforced breaking case can become a recurrence case when surface forcing operates while breaking onset can be delayed by similar surface forcing levels for some unforced breaking cases. An example where wind forcing stabilizes the motion of the wave group is case I with $N = 10$ and $s_0 = 0.089$. In this case, breaking occurs at $t/T = 126.4$ without wind forcing, yet breaking does not occur for this same initial wave group geometry when wind forcing of strength $\alpha_* = 0.0016$ is applied.

Another example of wind forcing delaying the breaking is case I with $N = 7$. Very strong surface forcing $\alpha_* = 0.0016$ does not change the initial steepness $s_0 = 0.099$ for marginal recurrence and only slightly accelerates the onset of breaking for the marginal breaking case of $s_0 = 0.10$, decreasing the time to breaking slightly from $t/T = 95$ for $\alpha_* = 0$ to $t/T = 94.9$. However, for a slightly larger initial steepness $s_0 = 0.11$ and the same surface forcing strength, the opposite behavior occurs, with the time to breaking increasing from $t/T = 70.8$ for $\alpha_* = 0$ to $t/T = 72.7$ and the steepness at breaking, $(ak)_{\text{br}}$, increasing from 0.3500 for $\alpha_* = 0$ to 0.3558 for $\alpha_* = 0.0016$. This suggests that the influence of the wind forcing in accelerating breaking onset may depend on the nonlinearity of the windsea.

Nevertheless, our results for wind forcing, summarized in Table 1, reinforce one of the central results of this study concerning the existence of a common breaking threshold δ_{th}. They confirm the critical aspect that even for extreme surface forcing, $\delta^{\max} < 1.30 \times 10^{-3}$ continues to apply for each recurrence case, while $\delta^{\max}$ exceeds 1.50×10^{-3} for all breaking cases that we investigated. Thus for surface forcing levels typical of open ocean conditions, the same critical threshold range of $(1.30\text{–}1.50) \times 10^{-3}$ for δ_{th} found for zero surface forcing appears to be applicable when wave-coherent surface forcing is operative.

4. Influence of a uniform surface shear

The actual depth distribution of the oceanic surface-layer shear current is a complex issue (e.g., Craig and Banner 1994), but following BT, we assumed a surface layer current $O(0.03U_{10})$ that decreased linearly over a depth of one significant wave height H_s. Here, U_{10} is the mean wind speed at the reference height of 10 m above the mean sea level and the H_s is related to the mean energy $\langle E\rangle$ of the waves by $H_s = 4\sqrt{\langle E\rangle}$. Thus we assumed a shear profile of the form $U(y) = \Omega y$, with $y = 0$ corresponding to mean sea level. The mean shear rate Ω was estimated using H_s calculated from the fully developed Pierson and Moskowitz (1964) windsea model for which

$$\langle E\rangle = 1.62 \times 10^{-3} g^2/(2\pi f_{\text{PM}})^4,$$

where

$$f_{\text{PM}} = 0.13 g/U_{10}.$$

For $U_{10} \sim 10$ m s^{-1}, this yields $\Omega \sim 0.12$ s^{-1}. Previously, BT investigated the effect of a strong background shearing current with $\Omega \sim 0.2$ s^{-1}. In this study, representative shearing current strengths up to $\Omega = 0.1$ s^{-1} were investigated. We were unable to define a robust reference velocity gradient for scaling Ω. However, when compared with a representative vertical gradient of the orbital motion of the initial carrier waves with typical initial steepness $(ak)_0$ of $O(0.1)$, it is easily shown that $\Omega = 0.1$ sec^{-1} corresponds to a nondimensional shear level $O(1)$. In any event, given the continually evolving nonlinear wave field with its fairly broad range of orbital speeds, we decided to retain the prescription of the dimensional shear level Ω (units: s^1). The addition of a background uniform shear is available as an option in the DP model code. After suitable scaling, this background shear was configured within the DP model and the corresponding local energy density E given by Eq. (6) of Part I was calculated. The details of this calculation are given in the appendix.

Unlike wind forcing, the presence of the shearing

TABLE 1. Summary of the maximum growth rates and key time scales from the numerical experiments for selected cases of interest with wind forcing and a uniform surface shear. δ^{max} is the maximum growth rate; t_{br} is the breaking time; t_{th} is the time when the growth rate $\delta(t)$ reaches the critical value $\delta_{th} = 1.50 \times 10^{-3}$; t_{max} and $t_{gr,max}$ are the times of the recurrence peak and the corresponding maximum growth rate; $t_{lead} = t_{br} - t_{th}$ is the lead time between $\delta(t)$ exceeding the threshold δ_{th} and the time of breaking onset; α_* and Ω show, respectively, the strength of the wind forcing and the shear current; s_0 is the initial steepness; N is the number of waves in the group; T is carrier wave period, R stands for recurrence; and B denotes breaking.

Cases	N	s_0	α_*	Ω	t_{th} (or $t_{gr,max}$)	t_{br} (or t_{max})	t_{lead}	$\delta^{max} \times 10^3$
I (R)	3	0.150	0	0	54.9T	57.5	—	0.69
I (B)	3	0.151	0	0	54.2T	55.5T	1.3T	3.30
I (R)	3	0.147	0.0016	0	62.4T	53.5T	—	1.10
I (B)	3	0.148	0.0016	0	54.9T	57.6T	2.7T	2.29
I (R)	3	0.143	0	0.1	49.1T	54.5T	—	1.15
I (B)	3	0.144	0	0.1	55.7T	57.1T	1.4T	1.78
I (R)	5	0.111	0	0	66.8T	82.7T	—	0.83
I (B)	5	0.112	0	0	80.3T	80.8T	0.5T	1.93
I (R)	5	0.107	0.0016	0	73.7T	86.6T	—	0.71
I (B)	5	0.108	0.0016	0	84.7T	85.0T	0.3T	3.98
I (R)	5	0.111	0.0001	0	66.8T	80.8T	—	0.84
I (R)	5	0.111	0.0002	0	66.9T	82.9T	—	0.87
I (B)	5	0.111	0.0003	0	82.5T	82.9T	0.4T	1.67
I (B)	5	0.111	0.0016	0	72.3T	74.6T	2.3T	3.98
I (B)	5	0.111	0	0.02	81.6T	82.6T	1.0T	2.06
I (B)	5	0.111	0	0.1	65.5T	69.2T	3.7T	2.67
I (B)	5	0.111	0.0016	0.02	70.1T	72.1T	2.0T	3.45
I (R)	5	0.107	0	0.1	73.1T	82.6T	—	1.11
I (B)	5	0.108	0	0.1	79.8T	80.5T	0.7T	2.52
I (B)	5	0.12	0	0	56.0T	60.5T	4.5T	3.27
I (B)	5	0.12	0.0016	0	55.5T	58.4T	2.9T	7.22
I (B)	5	0.12	0	0.1	50.7T	53.5T	2.8T	4.61
I (B)	5	0.12	0.0016	0.1	48.5T	51.4T	2.9T	4.18
I (R)	7	0.099	0	0	89.4T	96.7T	—	0.75
I (B)	7	0.100	0	0	94.3T	95.0T	0.7T	2.12
I (R)	7	0.099	0.0016	0	89.4T	98.9T	—	0.80
I (B)	7	0.10	0.0016	0	93.8T	94.9T	1.1T	2.24
I (R)	7	0.096	0	0.1	88.4T	95.8T	—	0.94
I (B)	7	0.097	0	0.1	95.8T	96.1T	0.3T	1.67
I (R)	7	0.099	0	0.02	81.5T	96.7T	—	0.84
I (B)	7	0.099	0	0.1	85.1T	87.0T	1.9T	3.60
I (B)	7	0.11	0	0	68.1T	70.8T	2.7T	6.76
I (B)	7	0.11	0.0016	0	69.1T	72.7T	3.6T	2.48
I (B)	7	0.11	0	0.02	67.2T	70.1T	2.9T	6.53
I (B)	7	0.11	0	0.1	64.0T	67.0T	3.0T	6.23
I (B)	7	0.11	0.0016	0.02	67.4T	70.4T	3.0T	8.03
I (R)	10	0.088	0	0	113.0T	126.0T	—	0.84
I (B)	10	0.089	0	0	126.0T	126.4T	0.4T	1.62
I (R)	10	0.090	0.0016	0	107.1T	118.0T	—	1.08
I (B)	10	0.091	0.0016	0	113.6T	116.1T	2.5T	4.39
I (R)	10	0.087	0	0.1	108.3T	123.8T	—	0.75
I (B)	10	0.088	0	0.1	118.4T	119.5T	1.1T	1.84

current considered here always destabilizes the wave group from recurrence to breaking and accelerates its onset. In some cases, an unforced case with recurrence can develop into a breaking case in the presence of a uniform surface shear layer. For example, for the marginally stable unforced case I with $N = 5$ and $s_0 = 0.111$, breaking occurs at $t/T = 82.6$ when a weak shear $\Omega = 0.02\ s^{-1}$ is present. Our results confirmed the BT findings that the surface shear current accelerates the onset of breaking. For example, for above case (i.e., case I with $N = 5$ and $s_0 = 0.111$), the breaking time decreases to $t/T = 69.2$ when a background linear vertical shear current with $\Omega = 0.1\ s^{-1}$ is applied. The corresponding evolution curves of $\mu(t)$, $\langle\mu(t)\rangle$, and $\delta(t)$ for this marginal recurrence, unforced case in the presence of shear $\Omega = 0.02$ and $\Omega = 0.1\ s^{-1}$, respectively, are shown in Fig. 4.

In a typical case where wind forcing delays the onset of breaking (i.e., case I with $N = 7$), the unforced marginal recurrence case with $s_0 = 0.099$ breaks at $t/T = 87$ when a background shear of strength $\Omega = 0.1\ s^{-1}$ is present. For $s_0 = 0.11$, the breaking time is $t/T = 70.8$ for $\Omega = 0$. The breaking onset time decreases to $t/T = 70.1$ for a weaker background shear with $\Omega = 0.02\ s^{-1}$ and to $t/T = 67$ for a stronger shear of strength $\Omega = 0.1\ s^{-1}$. Also, we found that shear reduces the

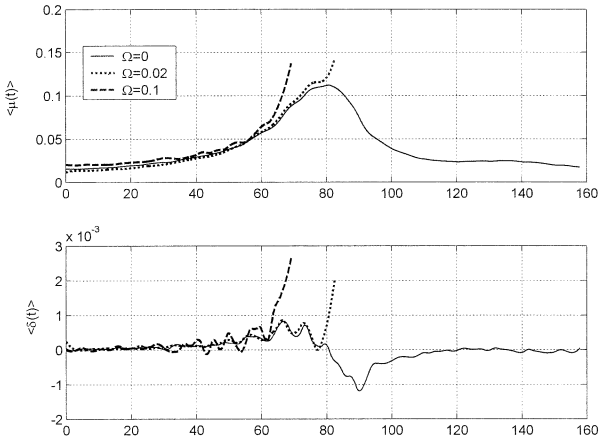

FIG. 4. As in Fig. 3 but showing the influence of shear on the long-term evolution of $\langle\mu\rangle$ and its associated growth rate $\delta(t)$ for case I with $N = 5$, $s_0 = 0.111$ and shear of strength $\Omega = 0$, 0.02, and 0.1 s^{-1}.

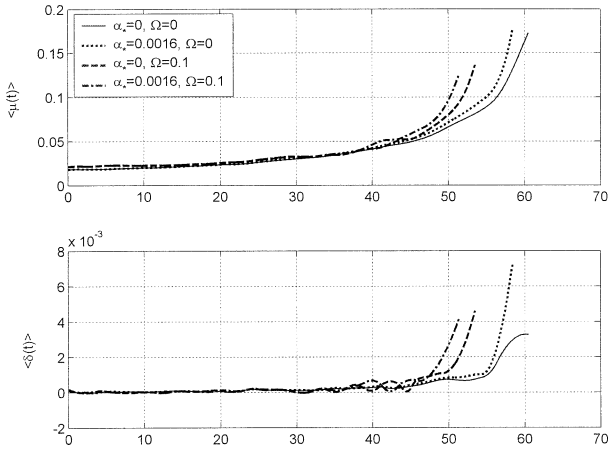

FIG. 5. As in Fig. 3 but showing the influence of wind forcing, shear, and combined wind forcing and shear on the long-term evolution of the mean trend $\langle\mu\rangle$ and its associated growth rate $\delta(t)$ for case I wave groups with $N = 5$, $s_0 = 0.12$.

critical initial steepness for marginal breaking. This means the critical initial steepnesses s_0^{Rc} and s_0^{Bc} become smaller when shear is present. For example, s_0^{Rc} and s_0^{Bc} reduce to 0.107 and 0.108, respectively, from 0.111 and 0.112 for the unforced cases of case I with $N = 5$ with a shear of strength $\Omega = 0.1$ s^{-1}. Corresponding changes in $\delta^{\max}$ are documented in Table 1 and reveal that the presence of shear significantly changes the behavior of wave group evolution and breaking process. For an unforced recurrence case, the presence of shear can make it break. For a breaking case, the presence of shear accelerates its onset and marginally modifies the value of $\delta^{\max}$. However, the onset of breaking is still determined by the common threshold δ_{th} value in the range $(1.30–1.50) \times 10^{-3}$.

5. Combined wind forcing and shear

It is appropriate to consider the effect of simultaneous shear and surface forcing as they usually act in unison. One example of the influence of a background shear for a case where surface forcing accelerates the onset of breaking is shown in Fig. 5. This is case I with $N = 5$, $s_0 = 0.12$, $\alpha_* = 0.0016$, and $\Omega = 0.1$ s^{-1}, for which breaking occurs at $t/T = 51.4$. In comparison, for this same case but with a shear of strength $\Omega = 0.1$ s^{-1} and zero surface forcing, breaking occurs at $t/T = 53.5$, while for the very strong surface forcing level $\alpha_* = 0.0016$ in the absence of shear, the breaking time increases to $t/T = 58.4$.

Another typical example of the influence of a background shear for a case where surface forcing delays the onset of breaking is shown in Fig. 6 for a weak shear with very strong wind forcing. In this example, $N = 7$, $s_0 = 0.11$, and a weaker background linear vertical shearing current of magnitude $\Omega = 0.02$ s^{-1} was used, as stronger shear masked the influence of the surface forcing. For strong surface forcing $\alpha_* = 0.0016$ in the presence of this background shear, breaking occurred at $t/T = 70.4$. Correspondingly, for very strong surface forcing $\alpha_* = 0.0016$ in the absence of shear, breaking occurred at $t/T = 72.7$. With the same weak background shear $\Omega = 0.02$ s^{-1} and zero surface forcing, the time to breaking decreased to $t/T = 70.1$. Thus the presence of a shearing current accelerates the onset of breaking, even if the shear is weak. This parallels the influence of shear on unforced cases discussed in BT. In passing, we noticed that surface layer shear tends to modify the surface profile and the evolution process of the nonlinear wave group more strongly than the wind forcing, although the modifications arising from either influence should be considered secondary in importance to the nonlinear wave group hydrodynamics. This is apparent from the properties of the representative case I examples summarized in Table 1.

Although a surface layer shearing current more

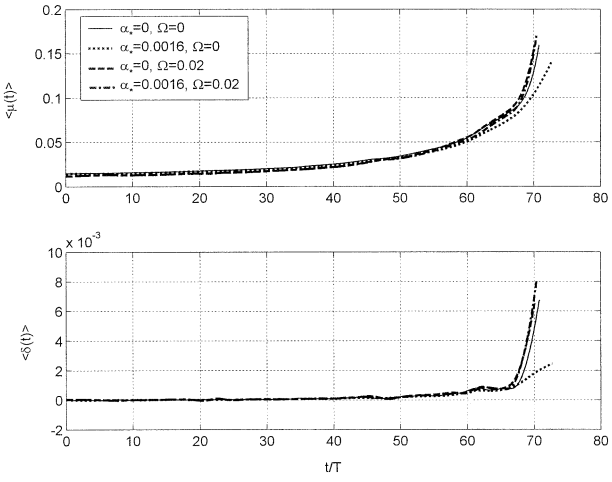

FIG. 6. As in Fig. 5 but for case I with $N = 7$ and $s_0 = 0.11$.

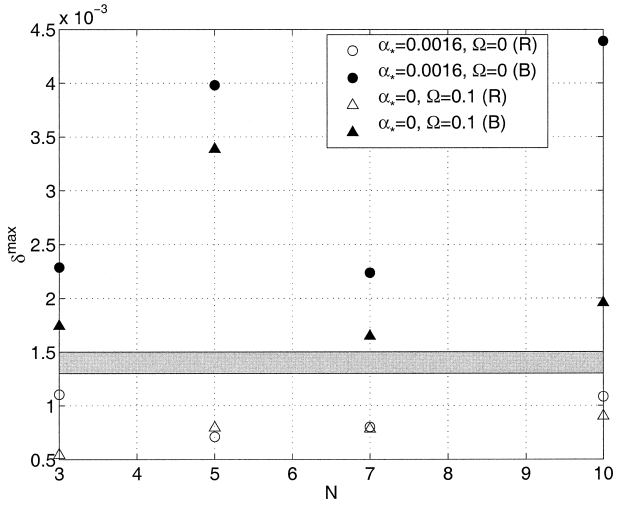

FIG. 7. Dependence of δ^{max} on N, the number of waves in the group for case I in the presence of a strong wind forcing or a uniform surface shear. Open and full circles correspond, respectively, to the marginal recurrence and marginal breaking cases of surface forcing with strength $\alpha_* = 0.0016$ in the absence of shear; open and full triangles, respectively, correspond to a shear level of $\Omega = 0.1\ s^{-1}$ zero wind forcing. The shaded region $\delta = (1.30 \times 10^{-3} - 1.50 \times 10^{-3})$ indicates the proposed common breaking threshold band for δ^{max}.

strongly modifies the surface shape and the evolution process than the wind forcing, the wave steepness at breaking was only modified (increased or reduced) slightly (i.e., by $\leq$5%) in the presence of a linear shear of strength $\Omega = 0.02$ or $0.1\ s^{-1}$. For example, $(ak)_{br}$ increased from 0.3069 to 0.3213 when the shear was reduced from $\Omega = 0.1$ to $\Omega = 0.02\ s^{-1}$ for case I with $N = 5$ and $s_0 = 0.111$. For case I with $N = 7$ and $s_0 = 0.11$, $(ak)_{br}$ changed to 0.3440 and 0.3513, respectively, from the unforced case where $(ak)_{br} = 0.3500$ when shears of strength $\Omega = 0.02$ and $0.1\ s^{-1}$ were present. These modifications to the breaking steepness are considerably smaller than the findings reported by BT for a stronger shear of $\Omega = 0.2\ s^{-1}$.

A summary of our results for δ^{max} and other parameters of interest for a number of representative shear and surface forcing cases is presented in Table 1. Of central importance is that the results validate our proposed critical average growth rate threshold range $\delta_{th} = (1.30–1.50) \times 10^{-3}$ for the diagnostic growth rate $\delta(t)$. Based on results in Table 1, Fig. 7 summarizes graphically the relationship between the growth rate δ^{max} and our proposed breaking threshold for various case I wave group configurations for cases of wind forcing of strength $\alpha_* = 0.0016$ in the absence of shear and shear of strength $\Omega = 0.1\ s^{-1}$ in the absence of wind forcing.

In section 5c of Part I, it was proposed that the strength of breaking events was proportional to the growth rate δ^{max}. Figure 8 shows comparative results for the influence of wind forcing and shear on the predicted breaking strength. This figure shows separately the marginal effect on the trend of our proposed breaking strength indicator δ^{max} due to wind forcing of strength $\alpha_* = 0.0016$ in the absence of shear and also for shear of strength $\Omega = 0.1\ s^{-1}$ in the absence of wind forcing. Results are shown for case I wave groups with

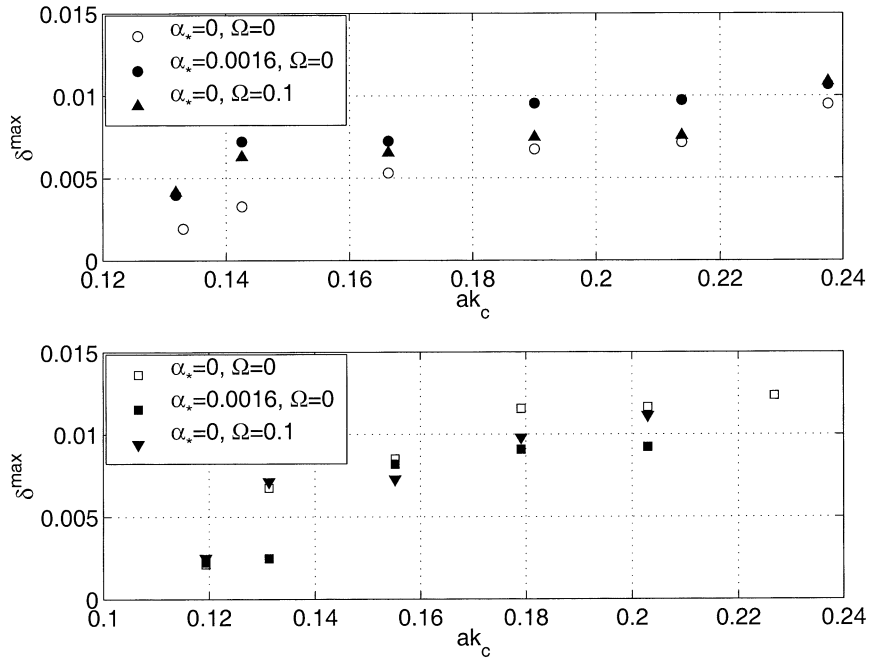

FIG. 8. The influence of wind forcing and shear on the maximum growth rate δ^{max} for case I breaking waves with different initial steepness ak_c: (top) $N = 5$ and (bottom) $N = 7$.

TABLE 2. Maximum growth rates and key time scales for breaking case I realizations with wind forcing or a background shear current, or with both of these effects operative, for different initial steepness s_0 and different N. Symbols in this table have the same meanings as in Table 1.

Cases	N	s_0	α_*	Ω	t_{th}	t_{br}	t_{lead}	$\delta^{max} \times 10^3$
I (B)	5	0.12	0.0016	0	55.5T	58.4T	2.9T	7.22
I (B)	5	0.14	0.0016	0	35.7T	40.4T	4.7T	7.25
I (B)	5	0.16	0.0016	0	26.9T	30.6T	3.7T	9.54
I (B)	5	0.18	0.0016	0	19.5T	23.2T	3.7T	9.73
I (B)	5	0.20	0.0016	0	15.7T	19.1T	3.5T	10.66
I (B)	5	0.12	0	0.1	50.7	53.5T	2.8T	4.61
I (B)	5	0.14	0	0.1	32.4T	36.1T	3.7T	5.91
I (B)	5	0.16	0	0.1	23.9T	27.3T	3.4T	7.41
I (B)	5	0.18	0	0.1	17.9T	21.5T	3.6T	7.63
I (B)	5	0.20	0	0.1	13.5T	18.7T	5.2T	9.46
I (B)	7	0.10	0.0016	0	93.8T	94.9T	1.1T	2.24
I (B)	7	0.11	0.0016	0	69.1T	72.7T	3.6T	2.48
I (B)	7	0.13	0.0016	0	47.6T	51.1T	2.5T	8.18
I (B)	7	0.15	0.0016	0	36.2T	39.5T	3.3T	9.49
I (B)	7	0.17	0.0016	0	28.1T	31.7T	3.6T	9.23
I (B)	7	0.10	0	0.1	82.6T	84.7T	2.1T	2.16
I (B)	7	0.11	0	0.1	64.0	67.0T	3.0T	6.23
I (B)	7	0.13	0	0.1	43.5T	47.4T	3.9T	6.84
I (B)	7	0.15	0	0.1	33.1T	36.7T	3.6T	8.35
I (B)	7	0.17	0	0.1	26.3T	30.3T	4.0T	10.35

$N = 5$ and $N = 7$ and suggest that the addition of wind forcing or shear does not produce significant variations from the trend of δ^{max} with increasing initial steepness ak_c for the unforced, irrotational case I wave groups that we investigated. Table 2 summarizes the corresponding maximum growth rates δ^{max}, t_{br}, t_{th}, and t_{lead}.

6. Conclusions

This study extends the scope of the results obtained for the unforced, irrotational cases of initial wave groups studied in Part I to investigate representative effects of wind forcing, shear, and the combination of these two additional upper ocean influences. Our findings were:

1) The presence of wind forcing and vertical shear typical of upper ocean conditions results in a similar evolution to recurrence or breaking and reinforces our conclusions of Part I. The associated nondimensional diagnostic parameter $\mu(t)$ evolves in a complex fashion, with a ''fast'' oscillation superimposed on a longer-term mean trend. As discussed in Part I, the trend of the local average of this parameter, $\langle\mu(t)\rangle$, encapsulates the observed systematic mean energy convergence toward (or away from) the maximum energy region within the wave group and this determines the ultimate breaking or recurrence behavior of the wave group. The fast oscillation, associated with the strong crest/trough asymmetry of the carrier waves, is believed to be primarily a kinematic effect.
2) Our results indicate that for a wide range of wave forcing and current shear, for representative examples of the three cases of initial wave group geometry we investigated, breaking or recurrence of deep water wave trains is still determined by the common threshold value δ_{th} in the range (1.30–1.50) $\times 10^{-3}$. This threshold, proposed in Part I for the nondimensional growth rate $\delta(t)$ of $\langle\mu(t)\rangle$ following the wave group maximum for unforced, irrotational wave groups, has been found to be applicable in the presence of these additional influences for the three classes of initial wave group structures we investigated.
3) In Part I, section 5c, it was suggested that the strength of breaking events may be controlled by the *mean* rate of convergence of energy at the group maximum immediately preceding breaking onset and reflected parametrically by the corresponding maximum value δ^{max} of $\delta(t)$ at the time of breaking onset. The addition of wind forcing and/or shear did not result in significant variations from the unforced trend of δ^{max} with increasing initial steepness for the set of case I realizations we investigated. In one case ($N = 5$), the addition of shear and wind forcing each tended to increase the maximum growth rates by a small margin, while in another case ($N = 7$), the addition of the same wind forcing or shear levels resulted in a comparable reduction. It remains for careful observations to confirm the correspondence between this proposed measure of breaking strength and actual energy losses.

Acknowledgments. The authors gratefully acknowledge the financial support of the Australian Research Council for this project. We also sincerely thank Prof. D. H. Peregrine, Prof. J. W. Dold, and Prof. Y. Agnon for allowing us to use their numerical codes.

APPENDIX

Calculation of the Local Energy Density E in the Presence of a Linear Shear Flow

For the special case of two-dimensional linear shear flow in the x–y plane, we can decompose the motion (u, v) into the superposition of a potential flow (u_0, v_0) and a uniform shear flow $(\Omega y, 0)$, where (x, y) are the horizontal and vertical coordinates respectively, and Ω is the constant vorticity. Upon substituting $(u, v) = (u_0, v_0) + (\Omega y, 0)$ into Eq. (6) of Part I, the local energy density E is given by

$$E = E_p + E_r, \tag{A.1}$$

where the potential flow contribution E_p is given by

$$E_p = \int_{-h}^{\eta} \frac{1}{2}\rho_w(u_0^2 + v_0^2)\, dy + \frac{1}{2}\rho_w g\eta^2, \tag{A.2}$$

and the rotational flow contribution is given by

$$E_r = \rho_w\Omega \int_{-h}^{\eta} u_0 y\, dy + \frac{1}{6}\rho_w\Omega^2\eta^3. \tag{A.3}$$

We note that bottom boundary terms that arise in E_p and E_r have been suppressed as they are not dynamically important in the present deep water wave context.

To calculate the influence of the uniform shear layer on the growth rate δ, the potential and rotational flow contributions E_p and E_r are needed. The methodology is presented below for obtaining the irrotational and rotational interior velocity fields corresponding to the free surface solution from the DP code for the case of a uniform background shear of strength Ω. From these velocity fields, the contributions E_p and E_r were calculated at each time step.

As discussed in detail at the beginning of section 4 of this paper, we assumed a uniform shear layer down to a mean depth of $y = -h$, with $h = 50$ m. As a practical lower limit in the calculation of E_r, we used $h = -8$ m. This was found to be necessary as the computed orbital velocity field developed very small, nonphysical residual mean offsets below this depth, where the orbital velocity was negligible even for the steepest waves for all cases investigated. The combination of these residual offsets with the large shear velocity at great depth produced spurious offsets in E_r. We checked this carefully by removing these mean offsets below -8 m and found negligible difference to the computed μ, $\langle\mu\rangle$, and δ values.

For the irrotational flow component, we work with the complex velocity $q_0 = df/dz = u_0 - iv_0$, where $f = \phi + i\psi$ in which ϕ and ψ are the velocity potential and the streamfunction corresponding to this irrotational flow component. The components of q_0 satisfy the familiar Cauchy–Riemann equations and the complex velocity q_0 is analytic with respect to $z = x + iy$ in the computational domain. The boundary condition $\phi_y = 0$ on the bed is satisfied by considering an image region, as shown in Fig. A.1a. In order to apply Cauchy's integral formula to calculate the value of q_0 at any interior point, following Fornberg (1980), the physical area with infinite fluid surface and its image is first transformed from the z plane into a finite closed region in the Z plane (see Fig. A.1b) by the conformal mapping:

$$Z(z) = e^{-i(2\pi/\lambda)z(x,y)}, \tag{A.4}$$

where λ is the spatial period of the wave group. In this investigation, λ was taken as 2π.

Since q_0 is periodic, it is transformed to a single-valued function $q_0(Z)$ in the Z plane that is analytic between S_1 and S_2 (see Fig. A.1 for notation).

At any interior point Z between S_1 and S_2, $q_0(Z)$ can be calculated by Cauchy's integral formula:

$$q_0(Z) = \frac{1}{2\pi i}\int_{S_1+S_2} \frac{q_0(Z')}{Z' - Z}\, dZ'. \tag{A.5}$$

The above equation can also be written as

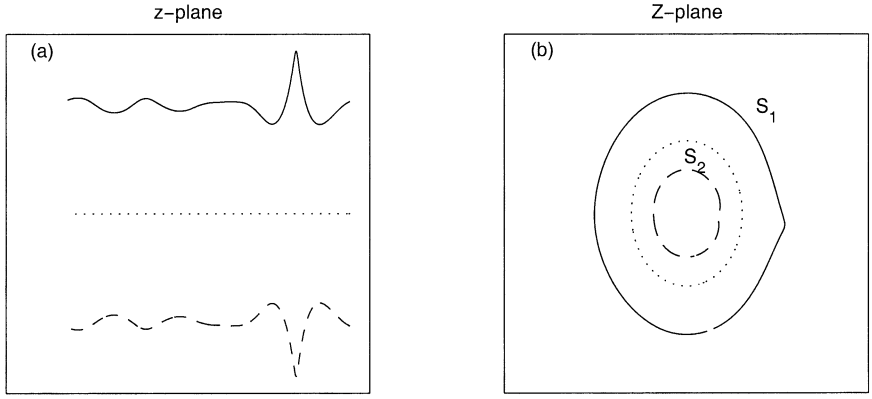

FIG. A1. Typical example of the conformal mapping $Z = e^{-i(2\pi/\lambda)z(x,y)}$. The impermeable flat bottom is shown as a dotted line. (a) Periodic wave train with $N = 5$ and group length $\lambda = 2\pi$ (solid line) and its image (dashed line) in the z plane. (b) The transformed region in the Z plane. The same line types used in (a) show the mapped water surface S_1, image surface S_2, and flat bottom, respectively.

$$\int_{S_1+S_2} \frac{q_0(Z') - q_0(Z)}{Z' - Z}\, dZ'$$
$$= \int_{S_1} \frac{q_0(Z_1) - q_0(Z)}{Z_1 - Z}\, dZ_1 + \int_{S_2} \frac{q_0(Z_2) - q_0(Z)}{Z_2 - Z}\, dZ_2 = 0, \quad \text{(A.6)}$$

where Z is an interior point between S_1 and S_2, Z' is on the contour S_1 or S_2, Z_1 is on the contour S_1, and Z_2 is on the contour S_2. We note that the integrand in (A.6) is never singular, no matter how closely Z approaches the boundaries. Following Fenton (1996), a numerical approximation is used here to transform the integral equation (A.6) into an algebraic equation by using the trapezoidal rules as follows:

$$\sum_{j=0}^{N_1-1} \left[\frac{q_0(Z_{1,j}) - q_0(Z_k)}{Z_{1,j} - Z_k} Z'_{1,j} - \frac{q_0(Z_{2,j}) - q_0(Z_k)}{Z_{2,j} - Z_k} Z'_{2,j} \right] = 0, \quad \text{(A.7)}$$

where $Z_{1,j} = Z(z_{1,j})$, $Z_{2,j} = Z(z_{2,j})$, $z_{2,j} = (z_{1,j})^* - 2ih$ (the asterisk denotes complex conjugate), $Z'_{1,j} = dZ_1(j)/dj$, and $Z'_{2,j} = dZ_2(j)/dj$. Here j is a continuous variable that takes on only integer values after the differentiation, and Eq. (A.7) then holds for each $Z_{1,j}$ and $Z_{2,j}$ with $j = 0, 1, 2, \cdots, N_1 - 1$, at which q_0 is known on the boundary. Also, Z_k with $k = 1, 2, \cdots, M$ is the set of M interior points where the flow details are sought.

The geometric coefficients $G^{(1)}_{kj}$ and $G^{(2)}_{kj}$ are introduced here as

$$G^{(1)}_{kj} = \frac{Z'_{1,j}}{Z_{1,j} - Z_k}, \qquad G^{(2)}_{kj} = \frac{Z'_{2,j}}{Z_{2,j} - Z_k}. \quad \text{(A.8)}$$

Then the Eq. (A.7) can be written as

$$\sum_{j=0}^{N_1-1} [(q^{(1)}_{0,j} - q_{0,k})G^{(1)}_{kj} - (q^{(2)}_{0,j} - q_{0,k})G^{(2)}_{kj}] = 0, \quad \text{(A.9)}$$

where $q^{(1)}_{0,j} = q_0(Z_{1,j})$, $q^{(2)}_{0,j} = q_0(Z_{2,j})$, and $q_{0,k} = q_0(Z_k)$. Solving for the $q_{0,k}$ gives

$$q_{0,k} = \frac{\sum_{j=0}^{N_1-1} (q^{(1)}_{0,j}G^{(1)}_{kj} - q^{(2)}_{0,j}G^{(2)}_{kj})}{\sum_{j=0}^{N_1-1} (G^{(1)}_{kj} - G^{(2)}_{kj})}. \quad \text{(A.10)}$$

Clearly, if the values of the complex velocity are known on the boundary and the geometric coefficients above have been calculated, the value of the interior complex velocity $q_{0,k}$ can be estimated for any arbitrary point Z_k.

As discussed in detail by Fenton (1996), the derivatives $Z'_{1,j} = dZ_1(j)/dj$ and $Z'_{2,j} = dZ_2(j)/dj$ can be calculated using a Fourier approximation as

$$Z'_{1,j} = \frac{i2\pi}{N_1^2} \sum_{n=0}^{N_1-1} Z_{1,n} d(j - n),$$
$$Z'_{2,j} = \frac{i2\pi}{N_1^2} \sum_{n=0}^{N_1-1} Z_{2,n} d(j - n), \quad \text{(A.11)}$$

where

$$d(0) = 0,$$
$$d(j - n) = i\frac{N_1}{2}(-1)^{j-n} \cot[\pi(j - n)/N_1] \quad \text{for } j \neq n. \quad \text{(A.12)}$$

Since

$$q^{(1)}_{0,j} = q^{(1)}_j - \Omega y_j,$$
$$q^{(2)}_{0,j} = (q^{(1)}_{0,j})^* = (q^{(1)}_j)^* - \Omega y_j, \quad \text{(A.13)}$$

where $q^{(1)}_j = u_j - iv_j = q^{(1)}_{0,j} + \Omega y_j$ is the value of the complex velocity $q = u - iv$ at the fluid surface point z_j and $(q^{(1)}_j)^*$ is the complex conjugate of $q^{(1)}_j$, Eq. (A.10) becomes

$$q_{0,k} = \frac{\sum_{j=0}^{N_1-1} [q^{(1)}_j G^{(1)}_{kj} - (q^{(1)}_j)^* G^{(2)}_{kj}]}{\sum_{j=0}^{N_1-1} (G^{(1)}_{kj} - G^{(2)}_{kj})} - \Omega \frac{\sum_{j=0}^{N_1-1} y_j (G^{(1)}_{kj} - G^{(2)}_{kj})}{\sum_{j=0}^{N_1-1} (G^{(1)}_{kj} - G^{(2)}_{kj})}. \quad \text{(A.14)}$$

Thus the interior velocity fields (u_0, v_0) can be computed based on (A.14), and E_p and E then can be calculated, respectively, by (A.2) and (A.1).

For deep water ($h \to \infty$), Eq. (A.14) reduces to

$$q_{0,k} = \frac{\sum_{j=0}^{N_1-1} q^{(1)}_j G^{(1)}_{kj}}{\sum_{j=0}^{N_1-1} G^{(1)}_{kj}} - \Omega \frac{\sum_{j=0}^{N_1-1} y_j G^{(1)}_{kj}}{\sum_{j=0}^{N_1-1} G^{(1)}_{kj}}. \quad \text{(A.15)}$$

Taking $\Omega = 0$, Eq. (A.15) reduces to the formula (A.9) of BT. Equation (A.14) can also be used in the calculations of the interior irrotational velocity fields for intermediate depth and shallow water waves by taking $\Omega = 0$.

REFERENCES

Banner, M. L., and O. M. Phillips, 1974: On the incipient breaking of small-scale waves. *J. Fluid Mech.,* **65,** 647–656.

——, and X. Tian, 1998: On the determination of the onset of wave breaking for modulating surface gravity water waves. *J. Fluid Mech.,* **367,** 107–137.

Bliven, L. F., N. E. Huang, and S. R. Long, 1986: Experimental study of the influence of wind on the Benjamin–Feir sideband instability. *J. Fluid Mech.,* **162,** 237–260.

Boccotti, P., G. Barbaro, and L. Mannino, 1993: A field experiment on the mechanics of irregular gravity waves. *J. Fluid Mech.,* **252,** 173–186.

Chen, G., and S. E. Belcher, 2000: Effects of long waves on wind-generated waves. *J. Phys. Oceanogr.,* **30,** 2246–2256.

Chu, J. S., S. R. Long, and O. M. Phillips, 1992: Measurements of the interaction of wave groups with shorter wind-generated waves. *J. Fluid Mech.,* **245,** 191–210.

Craig, P. J., and M. L. Banner, 1994: Modeling wave-enhanced turbulence in the ocean surface layer. *J. Phys. Oceanogr.,* **24,** 2546–2559.

Dold, J. W., and D. H. Peregrine, 1986: Water-wave modulation. *Proc. 20th. Int. Conf. on Coastal Engineering,* Taipei, Taiwan, ASCE, 163–175.

Donelan, M. A., 1987: The effect of swell on the growth of wind waves. *The Johns Hopkins APL Tech. Dig.,* **8,** 18–23.

——, 1999: Wind-induced growth and attenuation of laboratory waves. *Wind-over-Wave Couplings,* S. G. Sajjadi, N. H. Thomas, and J. C. R. Hunt, Eds., Clarendon Press, 356 pp.

——, M. S. Longuet-Higgins, and J. S. Turner, 1972: Whitecaps. *Nature,* **239,** 449–451.

Fenton, J. D., 1996: Exploiting boundary periodicity in the numerical solution of potential problems. *The Role of Mathematics in Modern Engineering: Proc. First Biennial Engineering and Mathematics Conf., Melbourne,* A. K. Easton and J. M. Steiner, Eds., Studentlitteratur, 565–576.

Fornberg, B., 1980: A numerical method for conformal mappings. *SIAM J. Sci. Statist. Comput.,* **1,** 385–400.

Holthuijsen, L. H., and T. H. C. Herbers, 1986: Statistics of breaking waves observed as whitecaps in the open sea. *J. Phys. Oceanogr.,* **16,** 290–297.

Komen, G. J., L. Cavaleri, M. Donelan, K. Hasselmann, S. Hasselmann, and P. A. E. M. Janssen, 1994: *Dynamics and Modelling of Ocean Waves.* Cambridge University Press, 532 pp.

Li, J. C., W. H. Hui, and M. A. Donelan, 1987: Effects of velocity shear on the stability of surface deep water wave trains. *Nonlinear Water Waves,* K. Horikawa and H. Maruo, Eds. Springer, 213–220.

Longuet-Higgins, M. S., 1984: Statistical properties of wave groups in a random sea state. *Philos. Trans. Roy. Soc. London,* **A312,** 219–250.

Millinazzo, F. A., and P. G. Saffman, 1990: Effect of surface shear layer on gravity and gravity-capillary waves of permanent form. *J. Fluid Mech.,* **216,** 93–101.

Phillips, O. M., 1977: *Dynamics of the Upper Ocean.* 2d ed. CUP, 336 pp.

——, and M. L. Banner, 1974: Wave breaking in the presence of wind drift and swell. *J. Fluid Mech.,* **66,** 625–640.

——, D. Gu, and M. A. Donelan, 1993: Expected structure of extreme waves in a Gaussian Sea. Part 1. Theory and SWADE buoy measurements. *J. Phys. Oceanogr.,* **23,** 992–1000.

Pierson, W. J., and L. Moskowitz, 1964: A proposed spectral form for fully developed wind seas based on the similarity theory of S. A. Kitaigorodskii. *J. Geophys. Res.,* **69,** 5181–5190.

Plant, W. J., 1982: A relationship between wind stress and wave slope. *J. Geophys. Res.,* **87,** 1961–1967.

Song, J.-B., and M. L. Banner, 2002: On determining the onset and strength of breaking for deep water waves. Part I: Unforced irrotational wave groups. *J. Phys. Oceanogr.,* **32,** 2541–2558.

Teles Da Silva, A. F., and D. H. Peregrine, 1988: Steep, steady surface waves on water of finite depth with constant vorticity. *J. Fluid Mech.,* **195,** 281–302.

Tulin, M. P., and T. Waseda, 1999: Laboratory observations of wave group evolution, including breaking effects. *J. Fluid Mech.,* **378,** 197–232.

Waseda, T., and M. P. Tulin, 1999: Experimental study of the stability of deep-water wave trains including wind effects. *J. Fluid Mech.,* **401,** 55–84.

Wright, J. W., 1976: The wind drift and wave breaking. *J. Phys. Oceanogr.,* **6,** 402–405.